Distinct Configurations of Antisite Defects in Ordered Metal Phosphates: Comparison between $LiMnPO_4$ and $LiFePO_4$

Sung-Yoon Chung,[1,2,*] Si-Young Choi,[3,†] Seongsu Lee,[4] and Yuichi Ikuhara[5,6]

[1]*Graduate School of EEWS and KAIST Institute for the Nanocentury, Korea Advanced Institute of Science & Technology (KAIST), Daejeon 305-701, Korea*

[2]*Nalphates LLC, Wilmington, Delaware 19801, USA*

[3]*Korea Institute of Materials Science, Changwon 641-831, Korea*

[4]*Korea Atomic Energy Research Institute, Daejeon 305-353, Korea*

[5]*Institute of Engineering Innovation, The University of Tokyo, Tokyo 113-8656, Japan*

[6]*Nanostructures Research Laboratory, Japan Fine Ceramics Center, Nagoya 456-8587, Japan*

(Received 6 December 2011; revised manuscript received 26 February 2012; published 7 May 2012)

By using a combination of aberration-corrected high-angle annular dark-field scanning transmission electron microscopy, *ab initio* density-functional theory calculations, and neutron powder diffraction techniques, We have found completely different configurations of the antisite exchange defects in $LiMnPO_4$ and $LiFePO_4$, with a random distribution of the exchange pairs without aggregation in the former and with zigzag-type clustering behavior preferred in the latter. Recalling the compositional analogy and identical crystal structure of the two metal phosphates, such unexpectedly distinct arrangement of the same type of point defects is a notable structural aspect.

DOI: 10.1103/PhysRevLett.108.195501 PACS numbers: 61.72.Bb, 68.37.Lp

Antisite cation exchange is one of the typical types of zero-dimensional lattice defects that are frequently observed in crystalline solids [1–3]. The significance of antisite defects is particularly apparent in many lithium-intercalated transition metal oxides, in which lithium and transition metal cations of similar size usually maintain a well-ordered framework. As lithium diffusion in such ordered oxides is highly anisotropic, the overall mobility of lithium ions can be greatly affected by cation exchange, even if the degree of exchange is minimal. Many extensive attempts have been made to observe the local variation in cation ordering in various lithium intercalation oxides [4–7].

Over the last decade, much attention has been devoted to lithium metal phosphates with an ordered olivine structure because they can serve as new cathode materials in rechargeable batteries [8,9]. One of the peculiar features of these phosphates is that the lithium diffusion in the lattice is one-dimensional along the *b* axis [10,11]. Consequently, control of both the concentration and distribution of antisite exchange defects is critical for improving lithium migration, as it directly affects the overall rate of (de)intercalation reactions. Although relevant antisite cation exchange can occur easily in phospho-olivines [12–14], as is true for a number of silicate minerals [1,15], no systematic comparison regarding the local distribution of antisite defects has been made between the ordered metal phosphates.

In this study, we definitively demonstrate the distinct configurational characteristics of antisite exchange pairs between two metal phosphates—there is a strong clustering behavior in $LiFePO_4$, whereas in $LiMnPO_4$ there is isolation and random distribution. For more accurate structural information on the antisite exchange defects in terms of the stable configurations, we utilized an experimental combination of atomic-scale direct probing with high-angle annular dark-field (HAADF) scanning transmission electron microscopy (STEM) and neutron powder diffraction together with *ab initio* density-functional theory (DFT) calculations. A recent first-principles study has verified very systematically that the antisite cation exchanges are always the most favorable intrinsic defects in $LiFePO_4$ at high temperature with low oxygen activity, irrespective of the Li/Fe nonstoichiometry [14]. Therefore, to focus on the antisite defects rather than other types of defects, all of the samples were prepared at sufficiently elevated temperature (700 °C) in a reducing atmosphere (high-purity Ar). Details for HAADF-STEM with spherical aberration correction (JEM-ARM200F, JEOL), neutron powder diffraction, and DFT calculations (CASTEP, Accelrys Inc.) are provided in the Supplementary Information.

Figure 1 shows the HAADF-STEM images of $LiFePO_4$ [Fig. 1(a)] and $LiMnPO_4$ [Fig. 1(b)] crystals annealed at 700 °C for 8 h, both of which were taken in the [010] projection. Schematic illustrations for the atomic arrangement of each unit cell are also represented in the same orientation. To clarify the contrast variation of atom columns, deconvolution filtering, which eliminates any background noise by the electron probe function, was performed on the raw images. Each filtered image is provided in color for a region indicated by a rectangle. As the intensity of each column in the HAADF mode depends on its average atomic number (Z) [16], the ordered arrays of bright contours in each image correspond to the Fe-P and

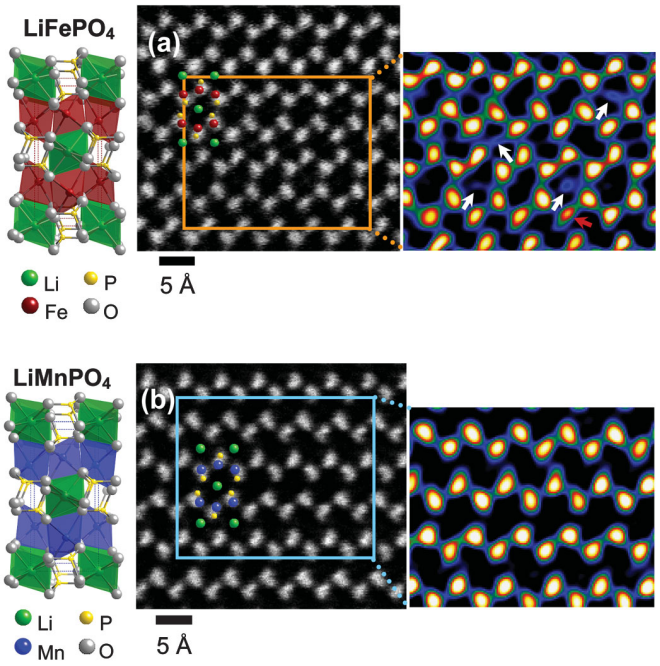

FIG. 1 (color). Comparative *Z*-contrast HAADF-STEM images in the *b* projection. (a) $LiFePO_4$ and (b) $LiMnPO_4$. The crystal structures of each unit cell in the [010] projection are illustrated. Schematics for the atomic array are also superimposed on the images for direct comparison. Each image processed by deconvolution is shown in color, clearly revealing that several Li columns with detectable intensity, as indicated by white arrows in (a) can be observed in $LiFePO_4$, whereas no such columns are found in $LiMnPO_4$ in (b) A red arrow denotes a Fe column with a relatively lower intensity.

Mn-P columns in the highly ordered olivine framework composed of Li in the edge-sharing oxygen octahedrons, and Fe or Mn in the corner-sharing oxygen octahedrons [17]. In good agreement with previous reports [5,18], Li columns with detectable intensity due to the presence of antisite Fe ions could be identified during the imaging of $LiFePO_4$, as denoted by white arrows in Fig. 1(a). Fe columns with lower intensity than others (for instance, the column indicated by a red arrow) were also found, as previously reported [12], although they were observed much less frequently than the Li columns at a detectable brightness.

In strong contrast to the observation of antisite defects in $LiFePO_4$, very few columns with antisite exchange were found for $LiMnPO_4$ crystals during atomic-scale analysis. Figure 1(b) shows a typical *Z*-contrast HAADF-STEM image of a $LiMnPO_4$ crystal in the [010] projection along with its deconvoluted image. Notably, there are no Li columns with any visible intensity in this image. More than 5500 Li columns were extensively investigated during the STEM analysis for statistical significance, and only four columns among these were found to have a detectable contrast (one example is presented in Figure S1 in the Supporting Information [19]). Based on the neutron powder diffraction and subsequent Rietveld refinement analysis, the overall Li−Mn exchange in the $LiMnPO_4$ specimen was determined to be ~2% (see supplementary Figure S2 and Table S1 for details [19]). Therefore, despite this amount of exchange defects, the considerably scarce detection of Li columns with visible intensity in HAADF-STEM directly indicates that the antisite cations in $LiMnPO_4$ do not exist in locally aggregated configuration, but rather, are dispersed in the entire crystalline lattice. If one recalls that the two phosphates have exactly the same crystal structure and a high chemical similarity, such distinct arrangement of the antisite cations in $LiMnPO_4$ is an unexpected finding.

To examine whether any other peculiar clustering behavior that is not observable in the [010] projection may appear in $LiMnPO_4$, additional HAADF-STEM analysis was performed in the other major projections in which the Li and Mn columns can be discriminated with sufficient point resolution. Figure 2 shows typical HAADF-STEM images of $LiMnPO_4$ crystals taken in the [001], [101], and [110] projections. Schematic illustrations

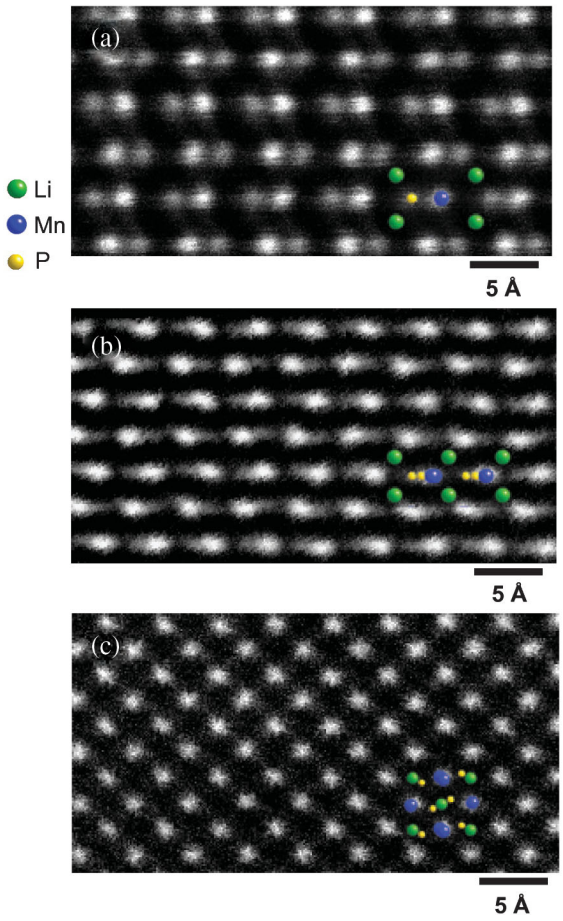

FIG. 2 (color). Additional series of HAADF-STEM images of $LiMnPO_4$ in different zone directions. The images were taken in the (a) [001], (b) [101], and (c) [110] projections. Note that there are no Li columns with bright contrast.

for atomic arrays in each projection are also superimposed on the images. The columns containing P can be identified near the Mn columns as small tails in the [001] and [101] projections. It is clear that no Li columns with visible contrast can be observed in these images. In particular, among more than 2300 Li columns in each case for the [001] and [101] projections, no columns that have detectable intensity were observed during the STEM analysis, supporting the finding that the antisite cations in $LiMnPO_4$ are randomly dispersed.

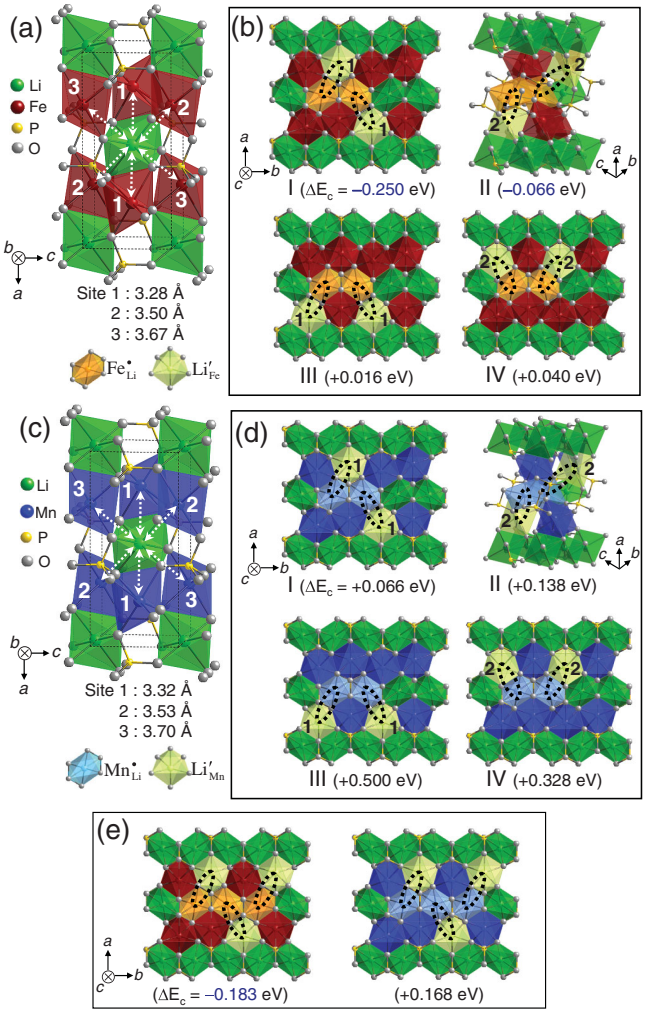

FIG. 3 (color). Schematic illustrations for unit cell structures and various configurations of antisite exchange pairs. (a) A unit cell structure of $LiFePO_4$ is illustrated in the b projection, showing the six nearest Fe neighbors from a Li site. The distances of three different nearest-neighboring sites (Sites 1, 2, and 3) are also indicated. (b) Four representative combinations (Cases I, II, III, and IV) of two antisite exchange pairs as a cluster are demonstrated. The numbers in parentheses denote the clustering energies for each case of clustering. (c) and (d) A unit cell structure and four combinations for the arrangement of two antisite exchange pairs in $LiMnPO_4$ are also shown in the same manner. Note that none of the clustering energies is negative. (e) Clusters composed of three exchange defect pairs in a zigzag configuration are depicted, indicating the substantially negative clustering energy for $LiFePO_4$ in contrast to the positive value for $LiMnPO_4$.

In good agreement with the results from the HAADF-STEM and neutron powder diffraction studies, the antisite exchange defects ($Li'_M - M^{\bullet}_{Li}$, where M = Mn and Fe), have been demonstrated theoretically to be major point defects with the lowest formation energy in $LiMnPO_4$ and $LiFePO_4$ [13,14]. To obtain a more detailed picture regarding the energetically stable configuration of the antisite defects, *ab initio* DFT calculations were conducted and the results compared with the atomic-level observations. For a systematic investigation, plausible binding behavior between Li'_M and $M^{\bullet}_{Li}$ was examined first before extending the calculations to multiply clustered exchange defects. As denoted by 1, 2, and 3 in Figs. 3(a) and 3(c), there are three different types of the nearest-neighboring M sites for each Li site, with the shortest distance between Li and neighbor M in Site 1. Herein, the "binding energy" is defined as the difference in formation energy when Li'_M and $M^{\bullet}_{Li}$ are separate from each other and are bound as a pair to the nearest neighbors. Table I lists the formation energies per antisite exchange pair, $Li'_M - M^{\bullet}_{Li}$ in $LiFePO_4$ and $LiMnPO_4$, along with the corresponding binding energies when all these neighboring sites are considered. From this set of calculations, strong binding behavior between Li'_M and $M^{\bullet}_{Li}$ is readily recognized in both phosphates. Compared with the separated configuration, the $Li'_M - M^{\bullet}_{Li}$ pairs bound to the nearest neighbors have a remarkable energy gain. While the antisite pair at Site 1 exhibits the lowest formation energy in $LiFePO_4$ among the three sites, Site 2 is most energetically favorable for pair formation in $LiMnPO_4$, with a very slight advantage over Site 1.

As a next step, the relative lattice stability was calculated when the bound $Li'_M - M^{\bullet}_{Li}$ pairs form a cluster. A number of combinations for cluster formation by the defects are geometrically possible even if only two antisite pairs are considered. However, based on the

TABLE I. Formation and binding energies of an antisite defect pair in $LiFePO_4$ and $LiMnPO_4$. (The lowest formation energies are represented in bold.)

Defect Pair	Formation Energy (eV)	Binding Energy (eV) ($E_{Site} - E_{separated}$)
	separated : 0.991	
$Li'_{Fe} - Fe^{\bullet}_{Li}$	bound in nearest neighbors	
($LiFePO_4$)	Site 1 : **0.454**	−0.537
	Site 2 : 0.551	−0.440
	Site 3 : 0.548	−0.449
	separated : 1.720	
$Li'_{Mn} - Mn^{\bullet}_{Li}$	bound in nearest neighbors	
($LiMnPO_4$)	Site 1 : 0.768	−0.952
	Site 2 : **0.758**	−0.962
	Site 3 : 0.802	−0.918

HAADF-STEM results demonstrating Li columns with visible intensity in the [010] projection, several combinations in which the $M_{Li}^{\bullet}$ ions of the two antisite pairs are placed in the nearest neighbor along the b axis can be selectively considered for efficient calculations. Figures 3(b) and 3(d) schematically show the defect arrangements describing some of the clusters composed of two antisite pairs. Each defect is represented in a different color: $M_{Li}^{\bullet}$ is in orange for $LiFePO_4$ and sky blue for $LiMnPO_4$, and Li_M' is in green for both. As illustrated in the schematics, two distinct categories for cluster formation are plausible. One is for clusters in which the two Li_M' defects are placed, respectively, in the upper and lower M-site rows in a zigzag manner (Cases I and II), and the other is for those in which they are in the same M-site row along the b axis (Cases III and IV).

For easier comparison of energy stabilities between each case, the "clustering energy (ΔE_c)" is defined as

$$\Delta E_c = E(\text{cluster}) - nE(\text{single pair}),$$

where E(cluster) is the formation energy of the entire n bound $Li_M' - M_{Li}^{\bullet}$ pairs when clustered and E(single pair) is the lowest formation energy of a single bound pair ($n = 2$ for the present calculations). Thus, a negative value of ΔE_c indicates that clustering between antisite pairs is energetically favorable over isolation. As indicated in Figs. 3(b) and 3(d), our calculations demonstrate that none of the ΔE_c for $LiMnPO_4$ is negative, whereas -0.250 and -0.066 eV are obtained as the clustering energy for $LiFePO_4$ in Cases I and II, respectively. Each value of ΔE_c for the plausible combinations is systematically summarized in Table II. Unfavorable clustering behavior of the antisite pairs, manifested as a positive ΔE_c in every case, is notable in $LiMnPO_4$, in contrast to the substantial advantage in formation energy in some of the zigzag-type clusters for $LiFePO_4$.

Such a difference in the stable arrangement of the antisite defects could be recognized more definitively when the lattice stability was calculated for clusters consisting of three bound pairs ($n = 3$). As Case I among the

TABLE II. Formation energies per single pair of antisite exchange defects and the resulting clustering energies for different cluster configurations.

Cluster Configuration [a]	Formation Energy per Single Pair (eV)	Clustering Energy (eV)
($LiFePO_4$) Li_{Fe}' $Fe_{Li}^{\bullet}$		
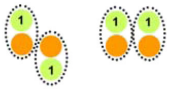	0.329 0.462	**−0.250** 0.016
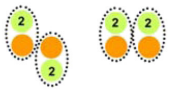	0.421 0.474	**−0.066** 0.040
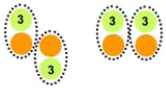	0.761 0.907	0.614 0.906
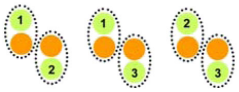	0.391 0.667 0.853	**−0.126** 0.426 0.798
($LiMnPO_4$) Li_{Mn}' $Mn_{Li}^{\bullet}$		
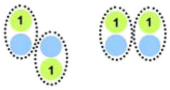	0.791 1.008	0.066 0.500
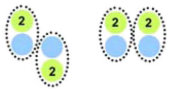	0.827 0.922	0.138 0.328
	1.704 1.903	1.892 2.290
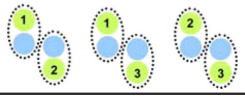	0.872 1.548 1.698	0.228 1.580 1.880

[a]Each cluster configuration is depicted in the c projection for consistency with Fig. 3. [Negative clustering energies are represented in bold number. Numbers in the schematic illustrations denote the nearest-neighboring M sites (Sites 1, 2, and 3), as shown in Figs. 3(a) and 3(c)].

zigzag-type clusters exhibits the lowest clustering energy, its derivative configuration has been selected in order to calculate triple-pair clustering, as illustrated schematically in Fig. 3(e). Even the negative ΔE_c (-0.183 eV) for the triplet in $LiFePO_4$ is very intriguing, confirming a strong tendency of this material towards clustering of the antisite defects. A higher ΔE_c ($+0.168$ eV) for the triplet than the doublet ($+0.066$ eV) in $LiMnPO_4$ also verifies the isolation characteristics of the antisite pairs.

Revealing an excellent agreement between the atomic-level STEM results and the *ab initio* DFT calculations, our study clearly demonstrates two distinct configurations of antisite exchange pairs in ordered olivine $LiMnPO_4$ and $LiFePO_4$. Despite the substantial concentration of the antisite defects, very few observations of the Li columns with detectable intensity in the HAADF-STEM images and positive clustering energies in $LiMnPO_4$ conclusively prove that there is a random distribution of bound $Li'_{Mn} - Mn^{\bullet}_{Li}$ pairs over the lattice without clustering. Thus, high entropy of mixing is expected, resulting in significant reduction of the total free energy of defect formation. By contrast, aggregation of antisite $Li'_{Fe} - Fe^{\bullet}_{Li}$ pairs as a cluster is consistently confirmed in $LiFePO_4$ not only by the experimental STEM analysis but also by the theoretical calculations of the comparative clustering energies. As depicted in Figs. 3(b) and 3(e), the energetically favorable cluster configurations in $LiFePO_4$ are based on $Fe^{\bullet}_{Li}$ ions in series along the b axis with Li'_{Fe} ions alternately placed in Fe rows in a zigzag manner.

HAADF-STEM image simulations in the [010] projection were also carried out for comparison with the experimentally obtained image in $LiFePO_4$. While notably visible contrast is easily detected in the Li columns with $Fe^{\bullet}_{Li}$ in the simulated images, no significant decrease of intensity is recognized in the Fe columns with Li'_{Fe} unless three bound $Li'_{Fe} - Fe^{\bullet}_{Li}$ pairs ($n = 3$) are clustered (see Figure S3 in the Supplemental Information [19]). Therefore, this zigzag-type defect configuration in the clusters, which is consistent with the image simulations, now reasonably explains why Li columns with visible contrast due to $Fe^{\bullet}_{Li}$ in $LiFePO_4$ were probed much more frequently than Fe columns of relatively lower intensity due to Li'_{Fe} when the HAADF-STEM images were taken in the b projection.

In summary, we have demonstrated that there are totally different configurations of antisite exchange defects in $LiMnPO_4$ and $LiFePO_4$, with random distribution of the exchange pairs without aggregation in the former and with strong clustering behavior in the latter. Despite the compositional analogy and identical crystal structure of the two metal phosphates, such a distinct configuration for the same type of point defects is very unusual and thus needs to be taken into careful consideration in order to avoid the retardation of lithium ion mobility in the lattice.

We thank Professor Yousung Jung for fruitful discussion on the thermodynamics of point defects. This work was supported by the National Research Foundation of Korea, Grants No. 2011-0003894, 2011-0004918, and No. 2011-0030297. S.-Y. C. was also financially supported by the GS project from RIST.

*Corresponding author.
nalphates@gmail.com
†Corresponding author.
youngchoi@kims.re.kr

[1] R. J. D. Tilley, *Defects in Solids* (Wiley, New York, 2008).
[2] M. J. Kramer, M. I. Mendelev, and R. E. Napolitano, Phys. Rev. Lett. **105**, 245501 (2010).
[3] M. K. Rasmussen *et al.*, Phys. Rev. Lett. **107**, 036102 (2011).
[4] K. Kang, Y. S. Meng, J. Bréger, C. P. Grey, and G. Ceder, Science **311**, 977 (2006).
[5] S.-Y. Chung, S.-Y. Choi, T. Yamamoto, and Y. Ikuhara, Phys. Rev. Lett. **100**, 125502 (2008).
[6] J. Lee, W. Zhou, J. C. Idrobo, S. J. Pennycook, and S. T. Pantelides, Phys. Rev. Lett. **107**, 085507 (2011).
[7] B. Xu, C. R. Fell, M. Chi, and Y. S. Meng, Energy Environ. Sci. **4**, 2223 (2011).
[8] A. K. Padhi, K. S. Nanjundaswamy, and J. B. Goodenough, J. Electrochem. Soc. **144**, 1188 (1997).
[9] S.-Y. Chung, J. T. Bloking, and Y.-M. Chiang, Nature Mater. **1**, 123 (2002).
[10] D. Morgan, A. Van der Ven, and G. Ceder, Electrochem. Solid-State Lett. **7**, A30 (2004).
[11] S.-I. Nishimura. G. Kobayashi, K. Ohoyama, R. Kanno, M. Yashima, and A. Yamada, Nature Mater. **7**, 707 (2008).
[12] S.-Y. Chung, Y.-M. Kim, S.-Y. Choi, Adv. Funct. Mater. **20**, 4219 (2010).
[13] G. R. Gardiner and M. S. Islam, Chem. Mater. **22**, 1242 (2010).
[14] K. Hoang and M. Johannes, Chem. Mater. **23**, 3003 (2011).
[15] L. M. Hirsch and T. J. Shankland, Geophys. J. Int. **114**, 21 (1993).
[16] P. D. Nellist and S. J. Pennycook, Ultramicroscopy **78**, 111 (1999).
[17] P. Tang and N. A. W. Holzwarth, Phys. Rev. B **68**, 165107 (2003).
[18] S.-Y. Chung, S.-Y. Choi, T. Yamamoto, and Y. Ikuhara, Angew. Chem., Int. Ed. **48**, 543 (2009).
[19] See Supplemental Material at http://link.aps.org/supplemental/10.1103/PhysRevLett.108.195501 for details.